

---

# High-Frequency Bulk Phase Modulator for Broadband Smoothing by Spectral Dispersion on OMEGA

High laser-irradiation uniformity is an important requirement for successful direct-drive inertial confinement fusion (ICF). Direct-drive laser-irradiation uniformity is achieved on OMEGA for different ranges of spatial frequencies using smoothing by spectral dispersion (SSD), polarization smoothing with distributed polarization rotators (DPR's), and multiple-beam overlap.<sup>1</sup> SSD significantly improves irradiation uniformity by rapidly shifting the laser speckle pattern generated by distributed phase plates (DPP's). A high-frequency electro-optic phase modulator produces a wavelength modulation that is subsequently converted by a diffraction grating into the angular deflection required to shift the speckle pattern. The low spatial frequency cutoff of the smoothing produced by SSD is determined by the maximum deflection of the beam. Extremely smooth, time-averaged intensity profiles are achieved on a time scale corresponding to the inverse bandwidth impressed by the phase modulator; thus, larger SSD bandwidths are desirable. Two-dimensional SSD (2-D SSD) extends the smoothing benefits of SSD by using two separate stages of bulk electro-optic phase modulators and gratings to deflect the laser speckle pattern in orthogonal directions.

For OMEGA, implementing a high-frequency modulator in the second direction of the 2-D SSD system is advantageous since the bandwidth from the second modulator is not dispersed until after the most-limiting spatial-filter pinhole, which is located in the large-aperture ring amplifier (LARA)<sup>2</sup> in the driver line. This constraint requires that high-frequency phase modulation be generated in a bulk electro-optic modulator to accommodate the dispersed bandwidth from the first modulator.

Design methods used to develop the current generation of 3.0- and 3.3-GHz bulk phase modulators<sup>3</sup> are directly relevant to higher-frequency designs, but several factors merit special attention in higher-frequency modulators designed to generate large SSD bandwidths. First, resonant designs are attractive since higher electric fields can be developed in the electro-optic material without expensive, high-power microwave sources. Velocity-matching the optical and microwave fields

is also important to achieve efficient optical phase modulation. Lastly, controlling FM-to-AM conversion at higher-modulation frequencies is a more difficult system problem.

A number of bulk electro-optic phase modulator designs are found in the literature.<sup>4-10</sup> An approximately 9-GHz modulator<sup>4</sup> implemented on the original 24-beam OMEGA laser system incorporated a lithium niobate (LiNbO<sub>3</sub>) crystal inside an evacuated, high- $Q$  microwave resonator, but it suffered difficulties coupling microwave power from the resonator mode into the crystal. Velocity-matched waveguide resonator designs<sup>5-7</sup> operate at microwave frequencies near the waveguide cutoff to match the optical and microwave phase velocities. This matching allows arbitrarily long interaction lengths to be used to achieve increased modulation efficiency. A quasi-velocity-matched concept<sup>8</sup> uses periodically poled lithium tantalate (LiTaO<sub>3</sub>) to approximately realize this same advantage with the added advantage of a TEM modulation field, but it suffers from the inherently lower  $Q$  factor of a micro strip resonator. An ~20-GHz dielectric resonator design<sup>9</sup> achieves a high  $Q$  factor, but the electric field distribution of the TM<sub>101</sub> resonant mode is poorly suited for 2-D SSD applications. Convenient coupling of microwave power into a resonator structure is also a critical design issue. Electric-probe<sup>6,9</sup> and magnetic-loop<sup>7</sup> coupling require that the resonator structure be partially air filled, but this reduces the maximum clear aperture. Cutoff-waveguide coupling eliminates this disadvantage and, in addition, offers the possibility of tuning the resonance frequency.<sup>10</sup>

Incorporating a higher-frequency phase modulator in the 2-D SSD system offers two approaches to improving irradiation uniformity on OMEGA. First, larger SSD bandwidths can be generated for a given number of FM sidebands and propagated through the laser system since less grating dispersion is required to achieve a single color cycle. Increased SSD bandwidths smooth laser irradiation faster. An asymmetric 2-D SSD configuration on OMEGA using phase modulators operating at 3.0 and ~10 GHz could achieve infrared bandwidths of  $1.5 \times 12 \text{ \AA}$ , respectively, to generate  $1 \times 1$  color cycles nominally.

This infrared bandwidth corresponds to a UV bandwidth of approximately 1 THz. To efficiently convert this infrared bandwidth to the ultraviolet, dual-tripler frequency-conversion crystals<sup>11</sup> (FCC's) must be implemented on all 60 OMEGA beams. This upgrade will be completed before the end of 1999.

Alternately, multiple SSD color cycles can be produced with a higher modulation frequency for a given grating design, and the same SSD bandwidth can be propagated without exceeding the beam divergence limit imposed by the laser system pinholes. Increasing the number of color cycles redistributes the beam nonuniformity to higher spatial frequencies and accelerates the smoothing at the mid-range spatial frequencies ( $\ell = 50\text{--}200$ ) that pose the greatest threat of seeding hydrodynamic instabilities in direct-drive implosions.<sup>1</sup> The current OMEGA FCC configuration can efficiently convert infrared bandwidths of  $1.5 \times 3.0 \text{ \AA}$  from modulators operating at 3.0 and  $\sim 10$  GHz to generate  $1 \times 3$  color cycles, respectively. Experiments utilizing both 1-THz UV bandwidth and multiple color cycle improvements are planned for OMEGA this year.

### High-Frequency Modulator Design

A velocity-matched, waveguide-coupled, LiNbO<sub>3</sub> dielectric resonator modulator design was selected for the 2-D SSD, high-frequency modulator application. A simple sketch of a generic cutoff-waveguide-coupled resonator<sup>10</sup> is presented in Fig. 78.1(a). A TE<sub>10</sub> mode of the input waveguide delivers microwave radiation to a high- $Q$ , TE<sub>10n</sub> standing-wave resonator formed by locating an electro-optic material in an air waveguide that would otherwise be below cutoff at the resonance frequency.

Velocity mismatches between the microwave and optical phase velocities in an electro-optic material reduce phase-modulation efficiency,<sup>12</sup> particularly at high modulation frequencies. In the resonant microwave cavities used for SSD bulk phase modulators, standing waves are impressed across the electro-optic crystal, which can be decomposed into fields co-propagating and counter-propagating with the laser beam. For this case, the velocity-mismatch reduction factor  $\beta$  is given by<sup>12</sup>

$$\beta = \frac{1}{2} \left| \frac{\sin(u_+)}{u_+} + \frac{\sin(u_-)}{u_-} \right|, \quad (1a)$$

$$u_{\pm} = \left( \frac{\pi f_m L}{c} \right) (\sqrt{\epsilon_3} \mp n_3), \quad (1b)$$

where  $\epsilon_3$  is the relative dielectric constant of the electro-optic crystal for polarizing the applied microwave field at the modulation frequency  $f_m$ ,  $n_3$  is the index of refraction of the crystal, and  $c$  is the speed of light in vacuum. The first term of Eq. (1a) accounts for the contribution of the optical beam interacting with the co-propagating microwave, while the second term is associated with the counter-propagating microwave field. The maximum effective interaction length  $\beta L$  for a 10.5-GHz LiNbO<sub>3</sub> modulator with no velocity matching is limited to approximately 2 mm, as shown in Fig. 78.2.

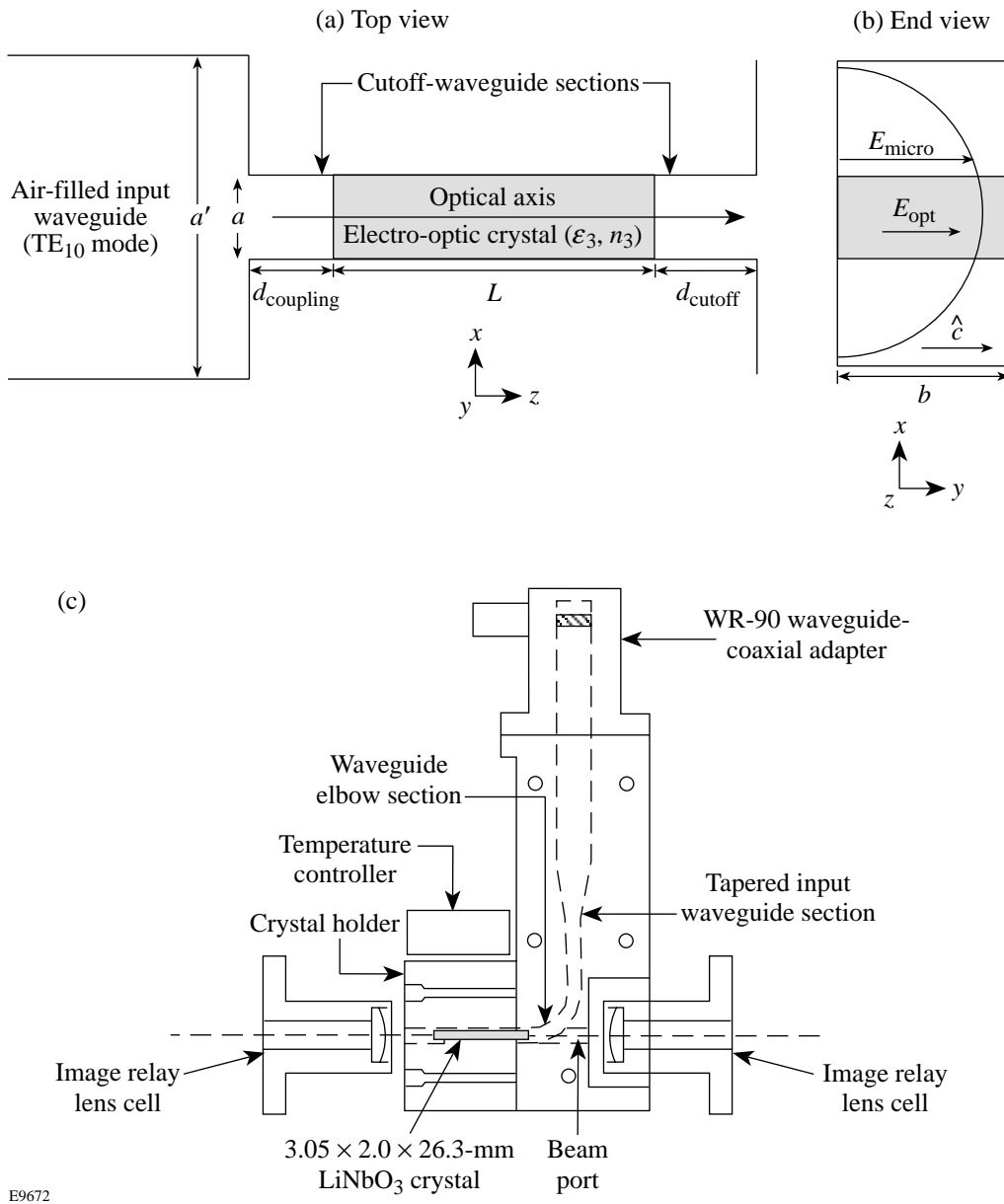
Velocity matching is achieved in the configuration shown in Fig. 78.1(a) by setting the width of the crystal,  $a$ , to adjust the microwave phase velocity in the waveguide geometry,

$$v_{\text{phase}} = \frac{c}{\sqrt{\epsilon_3} \sqrt{1 - (f_c/f_0)^2}}, \quad (2)$$

$$f_c = \frac{c}{2a\sqrt{\epsilon_3}},$$

to match the optical phase velocity in the electro-optic material,  $c/n_3$ , where  $f_c$  is the cutoff frequency of the waveguide section loaded with the crystal and  $f_0$  is the resonance frequency of the modulator. Figure 78.2 plots the effective interaction length as a function of crystal length for waveguide resonators with different degrees of velocity matching. For a perfectly velocity-matched design, the effective interaction length grows linearly with some modulation caused by the interaction with the counter-propagating microwave field. An almost negligible penalty is observed for a 10% velocity mismatch with a 26.3-mm crystal length shown in Fig. 78.1(c).

The height  $b$  of the crystal is arbitrary for a TE<sub>10n</sub> mode; however, minimizing  $b$  increases the electric field magnitude for a given microwave drive power and can eliminate spurious TE<sub>01m</sub> modes in the crystal that would divert microwave energy if mode-coupling mechanisms exist. The length of the electro-optic material determines the modulator resonance frequency based on the microwave phase velocity in the waveguide. A resonance exists for crystals that are an integer number of half-wavelengths, plus any phase shifts associated with the reflections at the cutoff-waveguide sections. For materials with a high dielectric constant, these phase shifts are generally small and only change the effective length of the resonator by about 1%.<sup>10</sup>



E9672

Figure 78.1

(a) Generic cutoff-waveguide-coupled resonator. The electro-optic crystal of length  $L$  is positioned in an air-filled, rectangular waveguide of width  $a$  and height  $b$ . The waveguide width sets the cutoff frequency above the modulator operating frequency in the air-filled sections, but below cutoff in the crystal. The cutoff-waveguide sections act as high reflectors for the standing waves inside the electro-optic crystal resonator. The input waveguide width  $a'$  supports traveling waves at the operating frequency that evanescently couple through the coupling distance  $d_{\text{coupling}}$ . (b) The microwave and optical electric fields,  $E_{\text{micro}}$  and  $E_{\text{opt}}$ , are oriented along the crystalline  $c$  axis to take advantage of the large electro-optic tensor element  $r_{33}$  in  $\text{LiNbO}_3$ . The beam size is small enough so that the variation of the microwave field in the  $x$  direction is only 15%. (c) A tapered input waveguide provides a transition from standard waveguide dimensions to dimensions required for critical coupling into the modulator crystal. A small beam port in the input waveguide bend provides optical access to the crystal but does not disturb the microwave input since it is significantly smaller than the microwave wavelength.

All SSD modulators designed and built at LLE have used  $\text{LiNbO}_3$ , which is a well-developed electro-optic crystalline material. Other electro-optic materials are commercially available and were considered for the new high-frequency modulator design, including  $\text{LiTaO}_3$ , potassium titanyl phosphate (KTP) and its crystal isomorphs, rubidium titanyl arsenate (RTA), and cesium titanyl arsenate (CTA). Relevant optical and microwave properties of these materials are reported in Table 78.I. A large electro-optic coefficient is obviously desirable, but the index of refraction and relative dielectric constant also play a significant role in maximizing the phase-modula-

tion performance, as indicated by the electro-optic figure of merit. The loss tangent is inversely related to the fundamental limit on the  $Q$  factor that can be achieved in a resonant design<sup>13</sup> since it represents the dielectric losses in each material. Lastly, the laser-damage threshold is an important performance parameter. Both bulk and surface laser-damage thresholds were measured for undoped  $\text{LiNbO}_3$  and are presented in Table 78.I. The surface finish of the samples limited the surface-damage threshold, while a lower bound on the bulk damage threshold was established that was limited by catastrophic surface damage. Doped samples of  $\text{Zn:LiNbO}_3$  and  $\text{MgO:LiNbO}_3$  showed poorer damage thresholds. RTA is a potentially attractive alternative possessing a high electro-optic figure of merit, a loss tangent almost four times lower than  $\text{LiNbO}_3$ , plus a lower dielectric constant that would facilitate approximately 20% larger crystal clear apertures. The optical quality of RTA, however, is not currently adequate for SSD applications since strong birefringence gradients are reported and the laser-damage threshold is significantly lower than commercially available  $\text{LiNbO}_3$ .

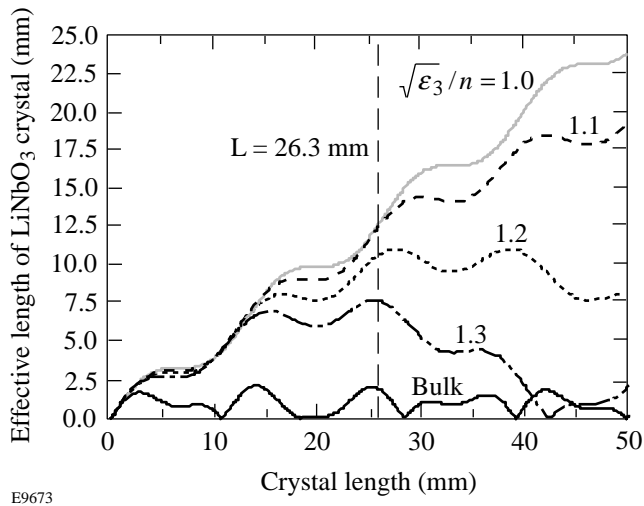


Figure 78.2 Effective interaction length with velocity matching in  $\text{LiNbO}_3$  modulators. Bulk modulator with no velocity matching (heavy solid line); perfect velocity matching essentially linear with respect to interaction length, with modulation due to interaction with counter-propagating microwave fields (light solid line); variations of velocity mismatch in 10% graduations (dashed lines).

Setting the beam size in a  $\text{TE}_{10n}$ -mode waveguide modulator requires a compromise between maximizing the uniformity of the phase-modulation depth across the beam and minimizing FM-to-AM conversion. The electric field of the standing wave varies across the transverse dimension, as shown in Fig. 78.1(b). This field distribution produces an index-of-refraction variation equivalent to a time-varying cylindrical gradient-index lens. Minimizing the SSD beam size to the central portion of the aperture minimizes this effect but increases the difficulty of SSD system imaging. The phase-modulated bandwidth dispersed by the SSD gratings must be carefully imaged to prevent FM-to-AM conversion resulting from propagation out of a grating image plane; otherwise,

Table 78.I: Electro-optic material properties.

	$\text{LiNbO}_3$ (Refs. 14,15)	$\text{LiTaO}_3$ (Refs. 16,17)	KTP (Ref. 18)	RTA (Ref. 16)	CTA (Ref. 16)
Crystalline type	uniaxial	uniaxial	biaxial	biaxial	biaxial
Electro-optic coefficient (pm/V)	$r_{33} = 28.8\text{--}30.8$	33	35.0	40.5	38.0
Index of refraction	$n_3 = 2.1561$ (extraordinary)	2.143	$n_z = 1.840$	$n_z = 1.890$	$n_z = 1.930$
Relative dielectric constant	$\epsilon_{33} = 23.7\text{--}27.9$	41.4–43	15.4	19	29
Loss tangent (at 10 GHz)	0.0015	0.001	0.70	0.0004	0.002
Electro-optic figure of merit $n_3^6 r_{33}^2 / \epsilon_r$ ( $\text{pm}^2/\text{V}^2$ )	3304	2548	2705	3935	2573
Laser-damage threshold ( $\text{GW}/\text{cm}^2$ )	>22 (bulk) >2.0 (surface)		>1	0.4	0.4

intensity modulation develops even from a perfectly FM-modulated beam according to

$$\frac{\Delta I}{I} \propto \delta_{\text{mod}} \cdot (\omega_{\text{mod}} d\theta/d\lambda)^2 z \propto \delta_{\text{mod}} \cdot \left(\frac{N_{\text{cc}}}{D_{\text{beam}}}\right)^2 z, \quad (3)$$

where  $\delta_{\text{mod}}$  is the phase-modulation depth,  $\omega_{\text{mod}}$  is the phase-modulation angular frequency,  $d\theta/d\lambda$  is the effective grating dispersion,  $z$  is the distance from the nearest image plane,  $N_{\text{cc}}$  is the number of color cycles impressed on the SSD beam, and  $D_{\text{beam}}$  is the beam diameter. Demagnifying the SSD beam to fit through the modulator increases the sensitivity to imaging errors and color separation of the dispersed FM beam on system optics that can lead to amplitude modulation. This is especially true for systems employing multiple color cycles.

The 10.5-GHz, waveguide-coupled LiNbO<sub>3</sub> modulator design [shown in Fig. 78.1(c)] includes four parts: a LiNbO<sub>3</sub> crystal, a crystal holder, a tapered input waveguide section, and a temperature controller. For a LiNbO<sub>3</sub> modulator operating at 10.5 GHz, the ideal crystal width to achieve velocity matching according to Eq. (2) sets  $a = 3.064$  mm. All four sides of the crystal are gold coated to form a standing-wave waveguide resonator that is approximately  $2 \cdot \lambda_{\text{microwave}}$  long, while the ends are antireflection coated for the SSD beam. The height is the smallest possible consistent with a 1.1-mm beam size chosen to limit the time-varying cylindrical phase error to a reasonable level.

The crystal holder and tapered input waveguide sections are machined from copper to maximize electrical and thermal conductivity and are gold plated to prevent oxidation of the copper. The high electrical conductivity of copper minimizes conduction losses in both the input waveguide and the waveguide resonator since the gold coatings on the crystal are only a fraction of a skin depth at 10.5 GHz. Good thermal conduction is also beneficial in maintaining a uniform temperature across the crystal.

The crystal holder is machined from three pieces of copper that confine the LiNbO<sub>3</sub> crystal on three sides while a copper foil holds it in place. This configuration ensures high-conductivity walls next to the crystal with no air gaps in the direction of the microwave electric field and minimal stress on the crystal. Active temperature control of the modulator crystal is planned to stabilize the resonance frequency and provide a limited range of tuning. The simulated results discussed below are based on the modulator operating at 50°C to provide a

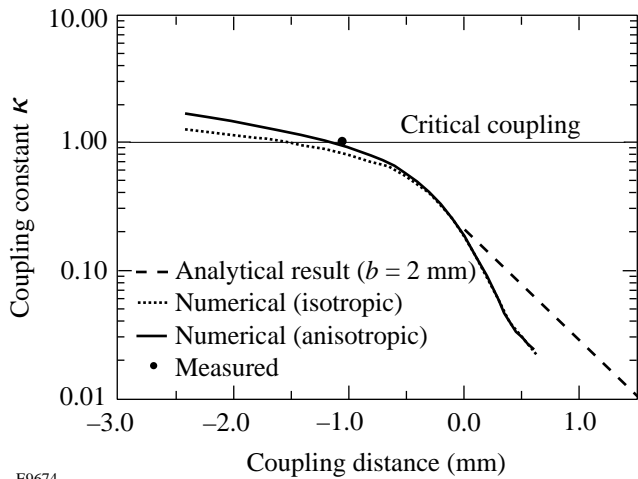
$\pm 20^\circ\text{C}$  range of temperature to accommodate uncertainties in the dielectric constant and crystal fabrication tolerances. A significant advantage of the modulator design is that the crystal holder can accept various crystal sizes designed to operate at different resonance frequencies.

The tapered input waveguide section transfers microwave power from a standard coaxial-to-WR-90 waveguide adapter to a 4-mm-high waveguide section suitable for coupling the microwave energy into the modulator crystal. The taper length is  $\lambda_{\text{microwave}}/2$  to minimize reflections associated with the waveguide discontinuities. A  $\lambda_{\text{microwave}}/2$ -long waveguide elbow is also included with a small beam port for optical beam access to the microwave input side of the crystal.

Maximizing microwave power transfer into a cutoff-waveguide-coupled resonator at resonance is accomplished by adjusting  $d_{\text{coupling}}$  to vary the coupling coefficient,<sup>10</sup>

$$\beta_{\text{coupling}} = \frac{16}{\pi^3} \frac{Q_0}{L_{\text{eff}}} \frac{\frac{a'}{a} \cos^2\left(\frac{\pi a'}{2a}\right) \epsilon_r - \left(\frac{\lambda_0}{2a'}\right)^2}{\left[1 - \left(\frac{a'}{a}\right)^2\right]^2 \epsilon_r (\epsilon_r - 1)} \times \lambda_0 \sqrt{1 - \left(\frac{\lambda_0}{2a}\right)^2} \exp\left[-\frac{2\pi d_{\text{coupling}}}{a'} \sqrt{1 - \left(\frac{2a}{\lambda_0}\right)^2}\right], \quad (4)$$

to achieve critical coupling ( $\beta_{\text{coupling}} = 1$ ), where  $Q_0$  is the resonator  $Q$  factor,  $L_{\text{eff}}$  is the effective length of the LiNbO<sub>3</sub> crystal, and  $\lambda_0$  is the free-space microwave wavelength; the remaining dimensions are defined in Fig. 78.1(a). Critical coupling maximizes the power transferred into the resonator.<sup>19</sup> Equation (4) was derived assuming no reaction of the cavity field on the waveguide field and is valid only for positive coupling distances. Using this analytic expression, the coupling coefficient calculated for the modulator presented in Fig. 78.1(c) is plotted in Fig. 78.3, where it is seen that critical coupling is not achieved, even for  $d_{\text{coupling}} = 0$ . This results from the poor overlap between the input waveguide and crystal resonator modes, which is limited by the large mismatch between the input waveguide width and the small crystal width imposed by the velocity-matching constraint. Although Eq. (4) cannot be extrapolated to negative coupling distances, it strongly suggests that allowing the modulator crystal to extend into the input waveguide would achieve critical coupling.

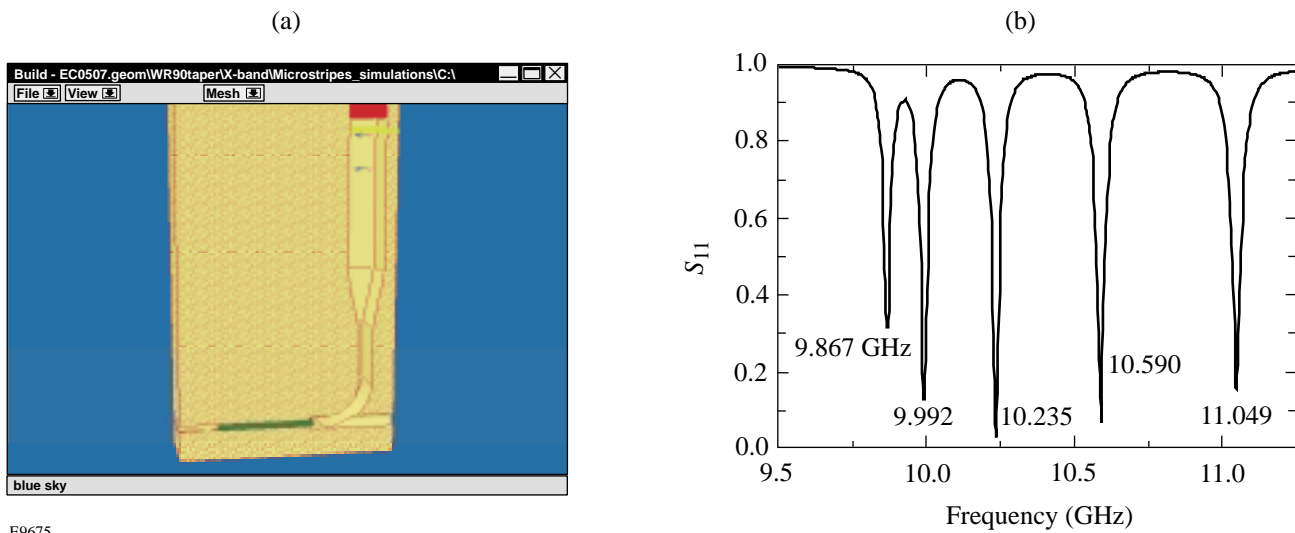


E9674

Figure 78.3 Coupling coefficient plotted versus coupling distance for waveguide-coupled LiNbO<sub>3</sub> modulator. The analytic values calculated from Eq. (4) are plotted in the dashed line only for positive coupling distances assuming the input waveguide and crystal heights are equal. Values from Micro-Stripes simulations modeling LiNbO<sub>3</sub> as an isotropic dielectric, as well as using the tensor values for the dielectric constant are plotted as dotted and solid lines, respectively. Critical coupling was experimentally observed for  $d_{\text{coupling}} = 1.07$  mm and plotted.

Accurately analyzing configurations where the crystal protrudes into the input waveguide was accomplished numerically using Micro-Stripes, a commercial three-dimensional electromagnetic analysis package.<sup>20</sup> Micro-Stripes yields both time- and frequency-domain electromagnetic solutions for arbitrary geometries, including tensor material properties such as the dielectric constant for materials like LiNbO<sub>3</sub>, which are difficult to treat analytically. A particular strength of this simulation package is that wideband frequency-domain results with fine resolution are obtained from a single time-domain simulation.

A typical Micro-Stripes model and the results from a simulation are shown in Fig. 78.4. All the geometric details and material properties of the modulator shown in Fig. 78.4(a) are represented in the model. In a simulation, an electromagnetic impulse is launched in the input waveguide, and the fields throughout the model are calculated as a function of time. Field values are saved at probe points for post-simulation analysis, including digital filtering, resolving incident and reflected waves, and transforming into the frequency domain. The complex reflection coefficient can be calculated as a function of frequency from the simulated forward and reflected microwave field components. The complex reflection coefficient can then be analyzed using a personal computer program QZERO<sup>19</sup> to yield the three important resonator parameters: the resonance frequency, the resonator  $Q$  factor, and the coupling coefficient.



E9675

Figure 78.4 Micro-Stripes numerical simulations. (a) The complete three-dimensional, anisotropic geometry of the LiNbO<sub>3</sub> modulator shown in Fig. 78.1(c) is modeled with spatial resolution required to yield accurate results; (b) the magnitude of the complex reflectivity plotted versus excitation frequency reflects the harmonic spectrum of the waveguide resonator formed by the LiNbO<sub>3</sub> crystal.

Micro-Stripes simulations were performed using an isotropic dielectric constant equal to the value along the designed microwave electric field direction ( $\epsilon_{33}$ ), as well as the tensor values available from the literature.<sup>15</sup> Simulations for a range of crystal positions were calculated and the coupling coefficient plotted in Fig. 78.3. For both cases, the coupling increases as the LiNbO<sub>3</sub> crystal protrudes farther into the input waveguide. Critical coupling is achieved for  $d \approx 1.2$  mm for the anisotropic calculation. The magnitude of the complex reflection coefficient plotted versus frequency for this crystal position is shown in Fig. 78.4(b). Nearly critical coupling into a high- $Q$  resonance is evident from the narrow, low-reflection feature representing the  $4 \cdot \lambda_{\text{microwave}}/2$  mode of the crystal resonator. Another feature evident from Fig. 78.4(b) is that the modulator can be optimally coupled for any of the other resonances to access even higher modulation frequencies; however, given the fixed resonator geometry defined by the crystal, a velocity-mismatch penalty would be incurred.

Figure 78.5 shows the predicted variation of the resonance frequency  $f_0$  and the resonator  $Q$  factor over the same range of crystal positions for the  $4 \cdot \lambda/2$  resonance as covered in Fig. 78.3. The resonance frequency shows a relatively small variation, and the  $Q$  factor is essentially unchanged over the range of crystal positions producing significant microwave coupling into the crystal. Interestingly, the resonance frequency plotted in Fig. 78.5(a) initially decreases as the length of the crystal protruding into the input waveguide increases, after which it increases monotonically. The initial drop in

resonance frequency, as well as the initially widening differences between the isotropic and anisotropic simulations of the resonance frequency, indicate that the effective length of the resonator increases as the resonator fields extend into the input waveguide and the fields distort near the crystal input. This field distortion introduces electric field components that interact with the higher dielectric constant ( $\epsilon_{11}$ ) in the  $x$  and  $z$  directions. After reaching minima, values for the resonance frequency for both cases increase at the same rate since the crystal length inside the crystal holder decreases. For positive values of the coupling distance  $d_{\text{coupling}}$ , the predicted resonance frequency approaches the value characteristic of the crystal loaded in an infinitely long, cutoff waveguide. The predicted  $Q$  factor in Fig. 78.5(b) also increases since the coupling losses into the input waveguide rapidly decrease, as seen in Fig. 78.3.

### Modulator Performance

Microwave measurements of the X-band modulator and adjustments to optimize coupling were performed using a microwave vector network analyzer (HP Model 8720B). As designed, the length of the crystal protruding into the input waveguide was set to maximize microwave coupling into the  $4 \cdot \lambda/2$  resonance. Excellent coupling was achieved for a coupling distance of  $-1.07$  mm. Within experimental uncertainties the measured return loss of  $-35$  dB represents critical coupling and is plotted in Fig. 78.3. Excellent agreement with predicted values of the coupling coefficient is observed.

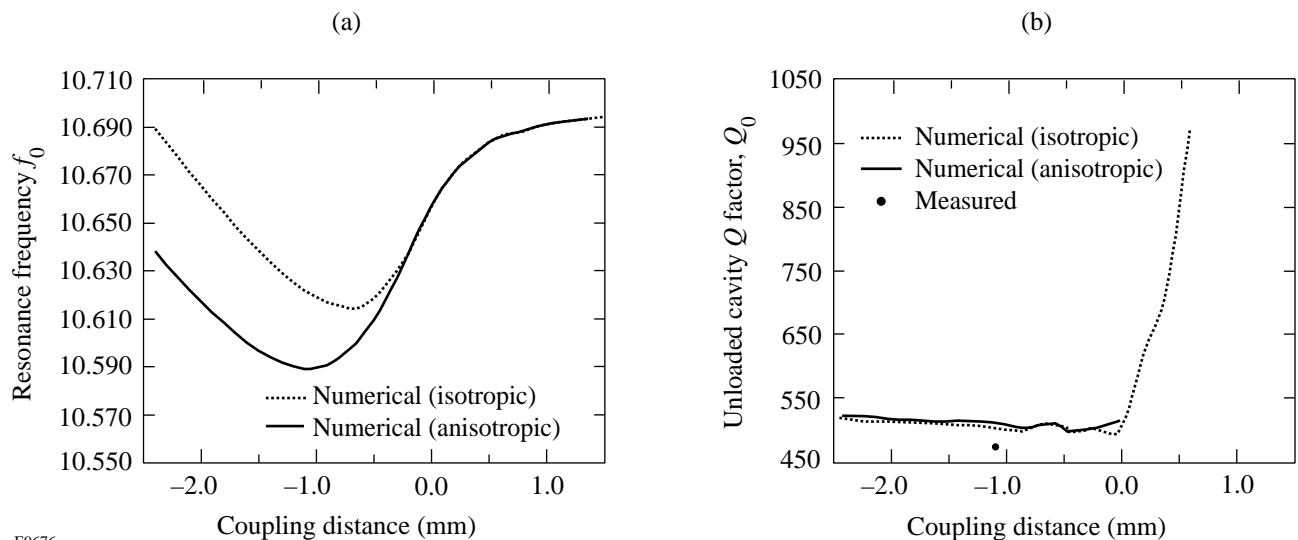


Figure 78.5

(a) Resonance frequency and (b)  $Q$  factor for cutoff-coupled, LiNbO<sub>3</sub> waveguide modulator.

The measured complex reflectivity of the modulator was also analyzed to evaluate the resonance frequency and  $Q$  factor. The measured resonance frequency at critical coupling is 10.412 GHz, which is 1.7% lower than predicted from the Micro-Stripes simulations. This discrepancy is attributed to three factors: First, the cutoff-waveguide cross section at the end of the crystal opposite the input waveguide was enlarged slightly to simplify alignment of the modulator in the SSD system, which would increase the effective length of the resonator and reduce the resonance frequency. Second, crystal fabricating tolerances resulted in slightly larger width and length dimensions that also increase the effective resonator length. Lastly, the actual dielectric tensor values for the LiNbO<sub>3</sub> crystal may differ from the literature values<sup>15</sup> used in the simulations. The measured  $Q$  factor plotted in Fig. 78.5(b) agrees well with the predicted values.

Experimentally, double-pass operation yields 1.95-Å SSD bandwidths with approximately 14.4 W of microwave power delivered to the modulator. This measurement of phase-modulation performance shows reasonable agreement with a simple estimate based on microwave measurements. The microwave energy stored in the resonator,  $E_{\text{stored}}$ , can be calculated from the definition of the unloaded  $Q$  factor,

$$Q_0 \equiv \omega_0 E_{\text{stored}} / P_{\text{in}},$$

where  $P_{\text{in}}$  is the power delivered to the modulator and  $\omega_0$  is the angular microwave frequency  $\omega_0 = 2\pi f_0$ . The stored energy  $E_{\text{stored}}$  can be related easily to the electric field strength inside the crystal,  $E_0$ , by approximating the field distribution with the mode of a TE<sub>10n</sub> resonator and spatially integrating to derive

$$E_{\text{stored}} = \epsilon_{33} / 8 (abL) E_0^2,$$

where  $\epsilon_{33}$  is the dielectric constant, and  $a$ ,  $b$ , and  $L$  are the crystal width, height, and length, respectively. These expressions can be combined with the expression for phase-modulation depth,<sup>3</sup>

$$\delta_{\text{mod}} = \frac{\pi \cdot \beta L \cdot n_3^3 r_{33}}{\lambda_{\text{opt}}} E_0,$$

where  $\beta L$  is the effective crystal length including velocity mismatch,  $n_3$  is the index of refraction,  $r_{33}$  is the electro-optic coefficient, and  $\lambda_{\text{opt}}$  is the optical wavelength. Using the measured values for  $Q_0$ ,  $a$ ,  $b$ , and  $L$ , literature values for  $\epsilon_{33}$ ,  $n_3$ , and  $r_{33}$ , a calculated value of  $\beta L = 0.95$  to account for some

velocity mismatch tolerance, a phase-modulation depth of 1.59 is calculated. For a single pass, this corresponds to an SSD bandwidth  $\Delta\lambda_{\text{single}} = 1.22$  Å, or a double-pass bandwidth  $\Delta\lambda_{\text{double}} = 2.44$  Å.

Additional SSD bandwidth can be achieved by increasing the number of passes through the modulator or increasing input power. Based on the measured performance, a double-pass configuration would require approximately 520 W of microwave drive power to generate 12 Å of phase-modulated bandwidth, while an active multipass scheme with four passes would require less than 130 W at the expense of greater system complexity.

## Conclusion

The design of an efficient, bulk phase modulator operating at approximately 10.5 GHz, which can produce substantial phase-modulated bandwidth with modest microwave drive power, has been presented. The waveguide resonator design employs an adapted form of cutoff-waveguide coupling and velocity matching to yield a simple, high- $Q$  microwave design with practical clear-aperture dimensions suitable for application in a 2-D SSD system. The design is easily scalable to other frequencies by simply changing the electro-optic crystal dimensions. The measured microwave performance of the modulator agrees well with performance predicted from fully anisotropic, three-dimensional numerical simulations.

## ACKNOWLEDGMENT

The authors acknowledge the support of the staff at the Laboratory for Laser Energetics of the University of Rochester without whose many years of diligent work the OMEGA laser system would not exist. This work was supported by the U.S. Department of Energy Office of Inertial Confinement Fusion under Cooperative Agreement No. DE-FC03-92SF19460, the University of Rochester, and New York State Energy Research and Development Authority. The support of DOE does not constitute an endorsement by DOE of the views expressed in this article.

## REFERENCES:

1. S. Skupsky and R. S. Craxton, *Phys. Plasmas* **6**, 2157 (1999).
2. Laboratory for Laser Energetics LLE Review **58**, 90, NTIS document No. DOE/SF/19460-17 (1994). Copies may be obtained from the National Technical Information Service, Springfield, VA 22161.
3. Laboratory for Laser Energetics LLE Review **68**, 192, NTIS document No. DOE/SF/19460-139 (1996). Copies may be obtained from the National Technical Information Service, Springfield, VA 22161.
4. Laboratory for Laser Energetics LLE Review **48**, 169, NTIS document No. DOE/DP40200-175 (1991). Copies may be obtained from the National Technical Information Service, Springfield, VA 22161.
5. G. Carter, *Appl. Phys. Lett.* **32**, 810 (1978).

6. T. F. Gallagher, N. H. Tran, and J. P. Watjen, *Appl. Opt.* **25**, 510 (1986); N. H. Tran *et al.*, *Appl. Opt.* **24**, 4282 (1985); T. F. Gallagher and J. P. Watjen, U.S. Patent No. 4,733,397 (22 March 1988).
7. A. A. Godil, U.S. Patent No. 5,414,552 (9 May 1995).
8. F.-Z. Guo *et al.*, *IEEE J. Quantum Electron.* **33**, 879 (1997).
9. A. A. Godil *et al.*, *Opt. Lett.* **16**, 1765 (1991).
10. E. Bonek *et al.*, *AEU* **32**, 209 (1978).
11. A. Babushkin, R. S. Craxton, S. Oskoui, M. J. Guardalben, R. L. Keck, and W. Seka, *Opt. Lett.* **23**, 927 (1998).
12. I. P. Kaminow and J. Liu, *Proc. IEEE* **51**, 132 (1963).
13. D. M. Pozar, *Microwave Engineering*, 2nd ed. (Wiley, New York, 1998).
14. Y. Ohmachi, K. Sawamoto, and H. Toyoda, *Jpn. J. Appl. Phys.* **6**, 1467 (1967).
15. R. S. Weis and T. K. Gaylord, *Appl. Phys. A* **37**, 191 (1985).
16. Crystal Technology data sheet, Palo Alto, CA 94303 (May 1993).
17. J. R. Teague, R. R. Rice, and R. Gerson, *J. Appl. Phys.* **46**, 2864 (1975).
18. Crystal Associates data sheet, Waldwick, NJ 07463 (May 1996).
19. D. Kajfez, *Q Factor* (Vector Fields, Oxford, MS, 1994).
20. Micro-Stripes<sup>TM</sup>, available from Sonnet Software, Inc., Liverpool, NY 13090.

